Direct Observation of Nanoparticle Superlattice Formation by Using Liquid Cell Transmission Electron Microscopy

Jungwon Park,[†,‡] Haimei Zheng,[‡] Won Chul Lee,[§] Phillip L. Geissler,[†,#] Eran Rabani,[⊥] and A. Paul Alivisatos[†,‡,*]

[†]Department of Chemistry, University of California, Berkeley, California 94720, United States , [‡]Materials Sciences Division, Lawrence Berkeley National Laboratory, Berkeley, California 94720, United States , [§]Department of Mechanical Engineering, University of California, Berkeley, California 94720, United States , [#]Chemical Sciences Division, Lawrence Berkeley National Laboratory, Berkeley, California 94720, United States, and [⊥]School of Chemistry, The Sackler Faculty of Exact Sciences, Tel Aviv University, Tel Aviv, 69978, Israel

ABSTRACT

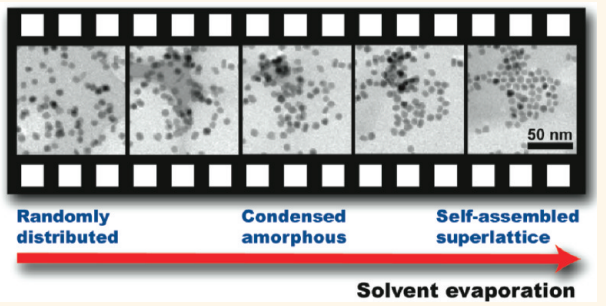

Direct imaging of nanoparticle solutions by liquid phase transmission electron microscopy has enabled unique *in situ* studies of nanoparticle motion and growth. In the present work, we report on real-time formation of two-dimensional nanoparticle arrays in the very low diffusive limit, where nanoparticles are mainly driven by capillary forces and solvent fluctuations. We find that superlattice formation appears to be segregated into multiple regimes. Initially, the solvent front drags the nanoparticles, condensing them into an amorphous agglomerate. Subsequently, the nanoparticle crystallization into an array is driven by local fluctuations. Following the crystallization event, superlattice growth can also occur *via* the addition of individual nanoparticles drawn from outlying regions by different solvent fronts. The dragging mechanism is consistent with simulations based on a coarse-grained lattice gas model at the same limit.

KEYWORDS: nanoparticle · self-assembly · *in situ* liquid cell TEM · platinum · and coarse-grained modeling

Colloidal nanoparticles (NPs), also known as artificial building blocks, provide an ideal model system to study crystallization from the nanometer scale to larger size scales.[1] Recently, the 2-D assembly of NPs on large substrates has shown potential as an alternative to top-down fabricated devices in energy harvesting and optoelectronic device applications. These colloidal NPs often provide homogeneous, intrinsically tunable materials with respect to their composition, size, and shape. Additionally, the process relying on NP assembly is relatively more facile.[2−4] Most NP assemblies, however, are formed under empirically optimized, perhaps uncontrolled, drying conditions. In this regard, understanding of fundamental mechanisms of assembly formation is desirable since it may provide the necessary insights that can help guide the creation of large scale arrays suitable for effective device architectures.

Solvent fluctuations, changes of the local density of the solvent on the length scale of the NPs during solvent evaporation, have determined the final morphology of NP assembly in previous experimental and theoretical studies.[5−13] It is more surprising when we note that different drying conditions of the same solvent change final patterns. Certain aspects of assembly can be explained by thermodynamics such as the sum of pairwise interactions.[1,14−17] Nonetheless, solvent fluctuations and resulting NP motions are expected to become more significant as the solvent continuously confines NPs into thin layers during evaporation.[7] Coarse-grained lattice-gas models have sought to explain how solvent fluctuations during the evaporation drive NPs to their final assembled structures,[7−10] yet experimental assessment on many of these predictions await the capability to capture real-time dynamics of NPs in nanometer scale resolution.

In-situ optical microscopy was used successfully to quantify the real time and real space crystallization and melting of colloidal microspheres, providing great insight into the forces between the particles and the factors influencing crystallization

* Address correspondence to APAlivisatos@lbl.gov.

Received for review October 5, 2011 and accepted February 23, 2012.

Published online February 23, 2012
10.1021/nn203837m

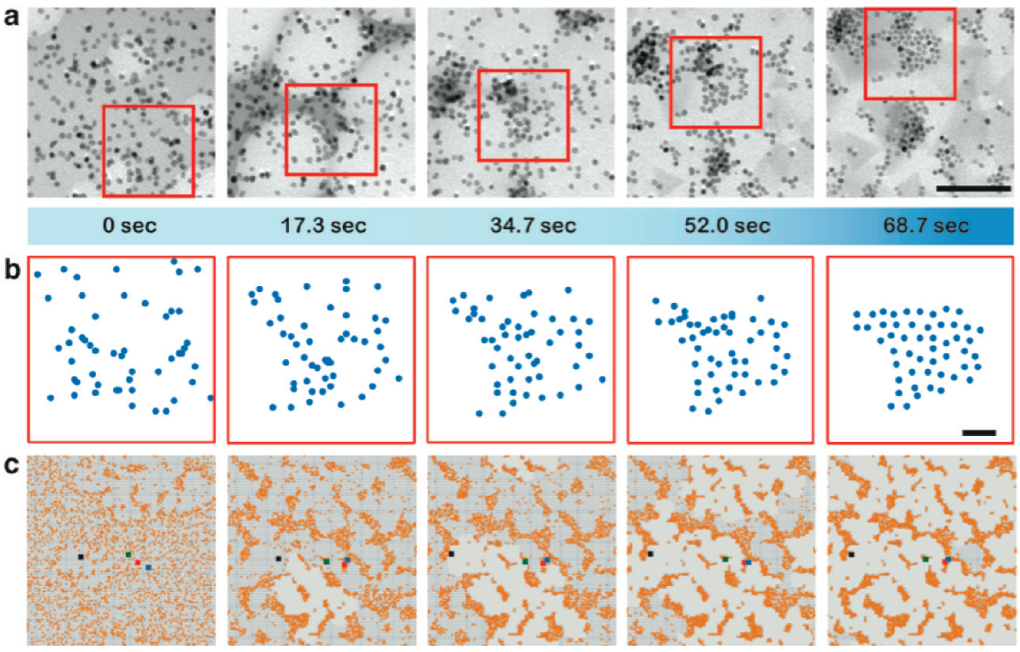

Figure 1. *In-situ* **observation of superlattice formation by liquid phase TEM and lattice gas modeling. (a) TEM snapshots from video 1 at different times. The scale bar is 100 nm. (b) Relative positions (corrected for thermal drift of the TEM sample) of selected 51 NPs taken from the red-squared area (120 nm × 120 nm) in Figure 1a. The scale bar is 20 nm. (c) Top view of assembly formation obtained from lattice gas modeling. Selected NPs are enlarged and colored with black, green, red, and blue to signify their motion time from left to right correspond to 15000, 25000, 25600, 26400, and 27000 in Monte Carlo (MC) units, respectively for coverage ρ = 30%, chemical potential $\mu = -3(^1/_4)\ \varepsilon_{//}$, temperature $T = \varepsilon_{//}$, and interfacial energies $\varepsilon_{ns} = (^1/_2)\ \varepsilon_{//}$, $\varepsilon_{/s} = \varepsilon_{//}$, and $\varepsilon_n = 2\varepsilon_{//}$. Image size corresponds to approximately 200 × 200 nm^2.**

and melting.[18−23] In NP assembly, where the size domain is below the diffraction limit of visible light, *in situ* atomic force microscopy, optical microscopy, and small-angle X-ray scattering have been the leading tools to study the nucleation and growth of NP clusters and the formation of superlattices at liquid/air and liquid/substrate interfaces.[4,24−28] However, microscopic details of how single NPs position at potential lattice points of a growing superlattice remain elusive. With the recent development of *in situ* liquid cells for transmission electron microscopy (TEM), it is now possible to extend these studies down to the nanoscale.[29−31]

RESULTS AND DISCUSSION

In this work, we employed liquid-phase TEM and observed the formation of Pt NP assemblies, *in situ*, at the substrate/solvent/vacuum interface. The technique provides the means to follow individual NP trajectories and to study in depth the evolution of the system to an ordered assembled state in real time. We demonstrate that during assembly Pt NPs were mainly driven by the strong capillary force of the evaporating solvent front, and possibly also by lateral immersion forces due to the hydrophilic nature of the solvent and the surface ligand of the NPs. We find that the assembly in given drying conditions of the *in situ* liquid cell proceeds by several distinct steps. In the first, NPs are contracted and condensed by the rapidly moving solvent into amorphous agglomerates, which span several monolayers in thickness. These agglomerates then expand laterally as they flatten to a single NP in thickness. At this point, additional local solvent fluctuations allow the system to relax to an ordered superstructure. These domains then grow by the subsequent addition of NPs, where capillary forces play an important role as well. Coarse-grained modeling provides a consistent picture with these experiments.

Pt NPs with 7.3 nm average diameter were synthesized by the reduction of ionic Pt precursors and dispersed in a 1:4 pentadecane: *o*-dichlorobenzene mixture with a small amount of oleylamine added in (see Methods for more detail).[32] The NP solution was then loaded into the liquid cell reservoirs, and the liquid cell was airtight for *in situ* TEM observation. This procedure provides approximately 30 min of viewing time. A schematic diagram of the liquid cell can be found in previous reports (Supporting Information (SI)).[31,33] Figure 1 summarizes the NP assembly formation obtained from a typical *in situ* liquid TEM experiment (see also video 1 in the SI). The electron beam has been used not only as an imaging tool but also as a driving force to evaporate the solvent locally from the illuminated area. Domians of varying solvent thicknesses induced by the electron beam radiation can be seen as changes in contrast as time progresses with thinner areas appearing as lighter contrast and thicker areas appearing as darker contrast (Figure 1a). Solvent evaporation nucleates at several spots which show up as bright circles in the first image and continue to expand until the solvent is gone in the final image. Similar patterns were observed during the evaporation of water.[34]

We also tracked several NPs forming one large domain in the final stage. Their relative positions (corrected for thermal drift of the TEM, see SI for more details), corresponding to the red-squared area in the TEM images, are shown in Figure 1b, and in SI, Figure S2, and video 2.

It is important to note that the length scale of the final ordered assembly is limited by the observation process, and the fact that evaporation is initiated at multiple independent sites. Nonetheless, we can track the motion of every particle associated with one evaporation zone, and in this way decipher the critical steps of NP assembly. Assembly driven by a single larger evaporation front, such as often occurs by ordinary evaporation in lab experiments outside the TEM, would likely include the same microscopic effect of solvent fluctuation on NP motion determining the final assembly, pattern, and further evidence for this will be shown below.

The motion of the NPs was captured with camera frame speeds of 5 to 30 frames per second, in order to track individual NPs with adequate precision. The thickness of the liquid sample with NPs was limited to less than 100 nm. Under the current experimental setup, the NP Brownian motion was significantly suppressed. NPs in static and fluidic solutions such as these have previously been shown to be weakly bound near the surface due to an attractive potential between the surface and the particles.[33,35] The gap between two silicon nitride (SiNx) windows was controlled by the height of the indium spacer during the fabrication steps but the actual thickness of the liquid sample could be thinner than the desired gap size, since excess solvent (*o*-dichlorobenzene) was dried during the sample loading. In this regime, the NP motion is mainly determined by the formation of drying patches. As the drying patches expand, solvent fronts push the NPs to areas that are still wet by the solvent (Figure 1a and video 1). The interparticle distance continuously decreases until NPs eventually pack together in an ordered 2-D phase (Figure 1a,b).

This picture is also consistent with lattice-gas simulation results shown in Figure 1c (see also SI, Figure S3 and Figure S4) under low NP diffusivity, where in addition to diffusive motion, NPs can also move as a result of solvent dragging (complete description of the lattice gas model and the dynamics is explained in the Methods section, SI, and previous reports).[7−10] The results shown in Figure 1c illustrate several important points. In the limit where the self-assembled structures are determined by solvent fluctuations, dragging can provide a competing mechanism for NP assembly where the role of solvent fluctuation has been usually underestimated. In such systems, self-assembly has been mainly explained by enthalpic and entropic factors such as inter-NP interaction, depletion forces, and ligand bridging. However, the solvent front can drive the NPs sufficiently to form ordered arrays under

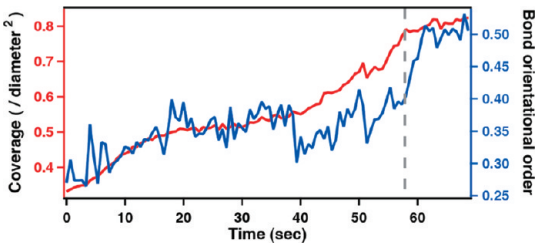

Figure 2. Surface coverage of NPs and the 2-D bond orientational order parameter, a measure of crystalline ordering, as a function of time. The self-assembly process is described with distinguished regimes (0−20 s, dragging NPs together by the evaporation solvent; 20−40 s, retarded solvent evaporation due to capillary condensation; 40−58 s, condensing NPs into dense amorphous structure; and 58−68.7 s, crystallization by flattening dense aggregatre to form ordered structure). Dashed line is shown to indicate that spike up of Ψ_6 occurs after coverage reaches plateau. Results are shown for the same trajectory of Figure 1b.

the condition where thermodynamics factors are not operative due to limited NP diffusion. The resemblance between the final morphologies obtained here and our previous simulations which ignored dragging (not shown)[9] is rather striking (see also Figure 3 for the experimental comparison). Despite the fact that in the absence of evaporation the NPs' mean square displacement (MSD) is quite low, dragging can move the NPs on length- and time-scales relevant for self-assembly, moving the particles across the detection window as they meet to form an ordered domain. The correlation between the morphologies obtained by the TEM experiments and the coarse-grained simulations further supports the importance of solvent dragging.

For each frame in Figure 1a, we selected 51 NPs (same particles as in Figure 1b) forming one domain at the final assembly stage and calculated their two-dimensional projected surface coverage within the minimum convex polygonal area containing all the selected NPs. In Figure 2 we show typical coverage plots corresponding to the trajectory shown in Figure 1b. The behavior of the surface coverage of the NPs can be described with several distinguished regimes. In the first stage (0 to 20 s), the interparticle distance decreases as NPs are dragged together by the evaporating solvent front. However, the rate of evaporation is retarded due to capillary condensation in the following time (20−40 s). As the interparticle distance decreases, the solvent trapped between NPs exposes less surface to the atmosphere and evaporates more slowly.[7,10] This leads to a retarded evaporation rate resulting in a slower increase of density. Then, density reaches its maximum level which indicates that the NPs have condensed, containing multiple layers of NPs (40−58 s). Upon completion of evaporation in the final stage (58−68.7 s), these multiple layers flatten out into partially ordered domains while maintaining a

maximum level of surface coverage. During the very last stage of assembly formation, solvent fluctuations compress the NPs onto the substrate to form a stable superlattice as the solvent dries completely.

In Figure 2 we also plot the 2D bond orientational order parameter as a function of time for the same trajectory to quantify crystalline ordering of the selected NPs.[20,23,36,37] The bond orientational order parameter is defined by

$$\Psi_6 = \left| \left\langle \frac{1}{nn} \sum_{k=1}^{nn} \exp(6i\theta_{jk}) \right\rangle \right|$$

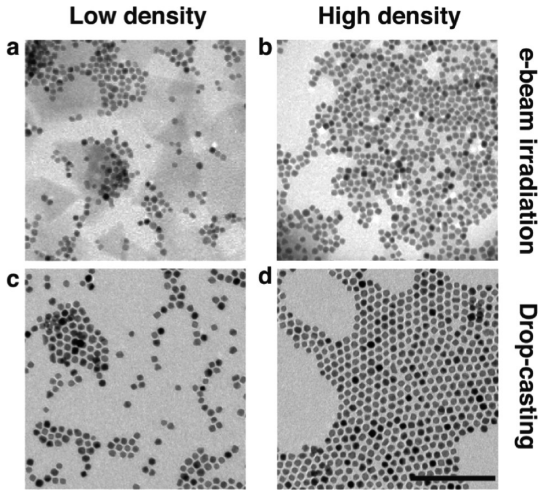

Figure 3. TEM images of NP assembly formed under electron beam irradiation (a,b) and drop casting (c,d) on SiNx TEM grid. The scale bar is 100 nm.

where θ_{jk} is the angle of the bond between particle j and its neighbor k, and nn is the number of nearest neighbors. Nearest neighbors were defined as NPs whose interparticle separation fell below a cutoff value that was derived from the first minimum of the radial distribution function (SI, Figure S5).[23] The value of ψ_6 is 1 for an ordered structure on a triangular lattice and near 0 for a disordered lattice. ψ_6 shows a small fluctuation before it abruptly spikes up around 57 s to a value of ~0.5. The maximum value of ψ_6 at the final stage is lower than 1 due to finite size effects and the intrinsic inhomogeneity of the NP size and shape. The most interesting observation is the abrupt increase of ψ_6 that occurs after the density of the NPs plateaus (58 s). This behavior occurs ubiquitously during the formation of such domains and coverage and ψ_6 plots for two more groups of NPs forming two separate domains in the final stage of self-assembly can be found in SI, Figure S6. This indicates that NPs form a very dense amorphous structure before crystallization. This is similar to a two-step crystallization mechanism observed in the nucleation of protein and micrometer-sized colloidal particles, where monomers first form an amorphous dense phase followed by crystallization.[38−41] Yet, the length scales and time scales are quite different, and thus, the mechanism and driving forces that lead to a two-step growth are likely to be different. Further understanding of the nature of the interparticle interaction in our system would lead to more insights. However, it is noteworthy that a similar two-step crystallization process has been demonstrated for the self-assembly of binary mixtures of colloidal NPs within a coarse-grained model.[42]

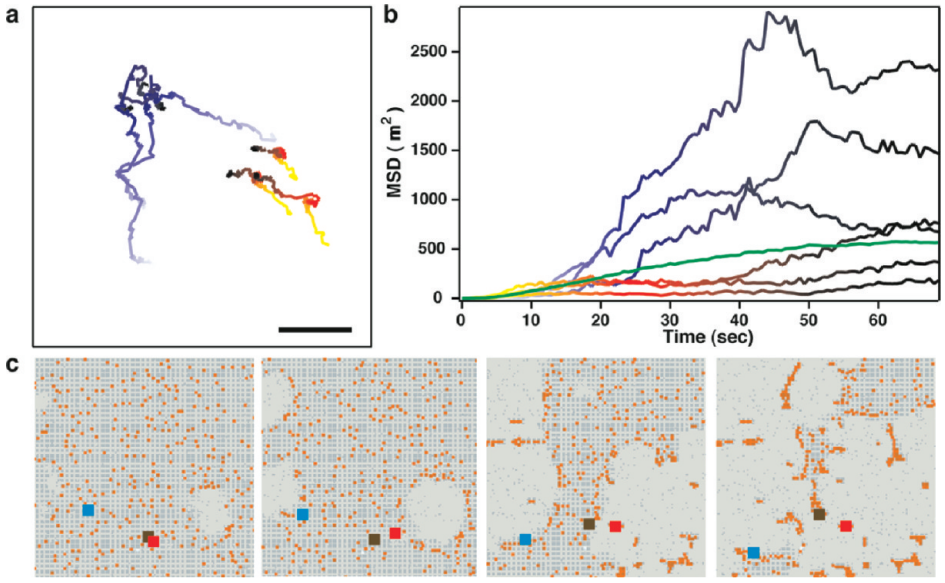

Figure 4. Individual NP motion in liquid phase TEM observation and lattice gas modeling. (a) Trajectories of selected individual NPs from Figure 1b for a time step of $\delta t = {}^1/_3$ sec. The time variable is labeled with blue and orange color scale for different types of trajectories. Black color indicates final stage of movement. The scale bar is 20 nm. (b) MSD of individual NPs shown in panel a with the same color scale along with the average MSD of the selected 51 NPs (green line). (c) Trajectories from lattice gas simulations. Selected NPs are enlarged and colored with red, brown, and blue to signify their motion. Time increases from left to right, for times (in MC steps) 1000, 1200, 1400, and 1600, respectively. Parameters are identical to those in Figure 1 for a coverage of ρ = 10%, chemical potential $\mu = -3({}^1/_8)\varepsilon_{/}$, and temperature $T = 2\varepsilon_{/}$. Image size corresponds to approximately 50 × 50 nm^2.

Once under view in the TEM, the 200 kV electron beam radiation interacts strongly with the liquid.[43] One effect we see clearly is beam-induced evaporation. Thus, a concern one may raise is related to the effects of the electron beam and TEM conditions on the self-assembly process. As a check, we have also compared the final assembled domain with superlattice structures formed by drop-casting on a SiNx membrane TEM grid. The SiNx membrane was prepared by the exact same fabrication process as for the SiNx windows of a liquid cell to ensure substrate interaction effects are identical. Figure 3 compares final domains from assemblies formed under electron beam irradiation and typical superlattice patterns resulting from a drop-casting experiment (see also SI, Figure S7 for simulated superlattice patterns with different coverage). Localized and heterogeneous drying condition in the TEM due to the presence of the electron beam results in a smaller length scale and less uniformity of the superlattice formed in the TEM compared to the drop-casting experiment. However, beyond similarity between overall superlattice patterns for the two cases, the identical interparticle distance indicates that the slightly overlapping NP ligand shells remain intact (SI, Figure S5).

We find that individual NPs follow different pathways to their ordered positions in the final assembled domain. Trajectories of selected NPs from Figure 1b and their MSD are shown in Figure 4a,b. Some NPs, labeled by scaled orange color, are continuously dragged by the solvent throughout the assembly formation over a small distance scale compared to the average MSD for the selected 51 NPs (green line). Other NPs, labeled by scaled blue color, follow a different pathway. They are dragged by the solvent at the beginning until they agglomerate into a sparse amorphous structure. Local fluctuations and further drying drive the NPs into their final ordered structure, as indicated by the decline in the slope of the MSD. Simulated trajectories in Figure 4c also show that individual NPs dragged by the solvent front follow different pathways. Three NPs that show distinct dynamics are enlarged and marked in red, brown, and blue squares. The blue NP is carried across a large distance by the solvent front, while the other NPs cover a relatively small distance. In addition, depending on how the solvent front recedes, NPs that are close to each other at early times before assembly occurs (red and brown squares) can end at quite different locations in the assembled domain. The individual NP trajectories are not only affected by the capillary forces imposed by the solvent but also by local fluctuations that lead to distinct dynamics for individual NPs.

In previous studies, convective transport of microparticles by capillary forces was found to be a main factor governing growth of domains as well as nucleation.[18,44] In Figure 5 (see also SI, video 3 and Figure S8)

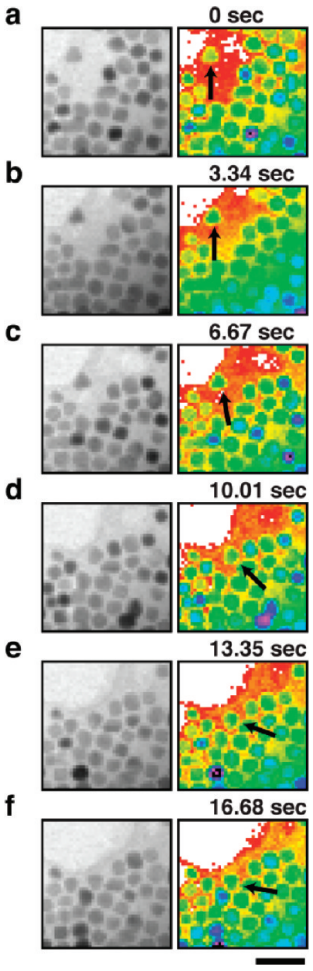

Figure 5. NP addition onto the domain of a superlattice. (a−f) Snapshots from video 3 at different times (left frames) and a corresponding color map with rainbow color scale (right frames). The contrast of rainbow color was calibrated such that white color corresponds to the dried area. The arrow indicates a NP that moves laterally and rotates until it adequately fills in a vacancy in the domain. The scale bar is 25 nm.

we show that this indeed is the case here as well by following the lateral and rotational motion of the incoming NP with triangle shape as it adds onto the domain. NPs first form small ordered domains. These domains then grow by the addition of individual NPs, where a freely moving NP, marked with an arrow, adds to an ordered array of NPs. The left column displays TEM images and the right column shows the corresponding images with a rainbow color overlay to clarify the solvent boundary and dried areas. The color scheme shows the white areas as low contrast regions due to drying of the solvent. Over the entire observation time NPs in the ordered array are blinking, which indicates the rapid changes in their crystal orientation along the direction of electron beam, demonstrating that they are still in wet conditions. The tagged NP approaches the array and fluctuates continuously upon contact until it fills the vacancy. While in ordinary nucleation theory the mobility of single particles is

Brownian-like, in the present case, it seems to be coupled strongly with the drying vapor front.

In-situ liquid cell TEM observation is the only method we know of that can offer the types of trajectories shown here, so it is desirable to determine if there are other additional effects besides evaporation that the beam could have on the sample. Possible effects include mechanical momentum transfer, atomic displacement, bond breakage, heating, radiolysis, and charging among numerous others.[43] We have seen no strong evidence that any of these processes alter the assembly.[33] We have calculated the beam induced heating, and it is very small.[33] We have calculated the degree of momentum transfer, and it too is very small.[33] It is more difficult to make any definitive statements regarding chemical changes induced by the beam. There is no question that the e-beam could be chemically perturbative, and it will require substantial more study to fully establish if this is happening. The close similarity in the final structures between those observed here and those obtained by standard evaporation techniques shows that at least the e-beam does not change the final outcome of the assembly process.

CONCLUSION

In this paper, we used a liquid phase TEM to image the drying-mediated self-assembly of NPs in real time. As the solvent evaporates under electron beam irradiation, NPs are dragged by the receding solvent front to form an ordered superlattice array. The superlattice formation is composed of several steps and actual crystallization takes place after the NPs are contracted into a dense disordered phase. In addition, domains can continue to grow by the addition of NPs that are dragged by capillary forces. Lattice gas simulation results provide a consistent picture when the motion of NPs is governed by solvent fluctuations and capillary forces rather than Brownian motion. Our work provides experimental tools needed to better understand the mechanisms of drying-mediated self-assembly at the level of single NP dynamics.

METHODS

Synthesis of Pt Nanoparticles and Preparation of Liquid Cell Sample. Pt NPs were prepared by following previously reported method with modification.[32] A total of 0.05 mmol of Pt ions ($(NH_4)_2$-Pt(IV)Cl_6, 80%; and $(NH_4)_2$Pt(II)Cl_4, 20%), 0.75 mmol of tetramethylammonium bromide, and 1.00 mmol of poly(vinylpyrrolidone) (in terms of the repeating unit; M_w = 29 000) were dissolved into 10 mL of ethylene glycol in a 25 mL round-bottom flask at room temperature. This solution was heated to 180 °C in an oil bath at 60 °C/min and kept at 180 °C for 20 min under argon flow and magnetic stirring. After formation of a dark brown solution, it was cooled to room temperature. Acetone (90 mL) was added and a black suspension was separated by centrifugation at 3000 rpm for 10 min. The black product was redispersed in 20 mL of ethanol and precipitated by adding an excess amount of hexane. This cleaning process was repeated two or three times. Resulting Pt NPs were dispersed in an excess amount of oleylamine for further ligand exchange reaction and refluxed overnight in an oil bath under mild stirring. NPs were separated from the solution by centrifugation at 14000 rpm for 30 min. Obtained Pt NPs were soluble in organic solvents. For *in situ* liquid cell experiment Pt NPs were dispersed in an organic solvent mixture (*o*-dichlorobenzene/pentadecane/oleylamine = 100:25:1 in volume ratio). As-prepared Pt NPs solution in a solvent mixture was loaded into two reservoirs of liquid cell by micropipet. The liquid sample was exposed to ambient conditions for a while to ensure that the *o*-dichlorobenzene dried out before sealing. Vacuum grease was applied on one side of a copper aperture grid with a hole size of 600 μm. The liquid cell was covered with a vacuum grease applied aperture grid for an airtight environment.

Coarse-Grained Lattice Gas Simulation. Simulations have been performed in 3D with a lattice gas Hamiltonian defined by

$$H = -\varepsilon_{\ell}\sum_{ij}\ell_i\ell_j - \mu\sum_i \ell_i - \varepsilon_n\sum_{ij} n_i n_j - \varepsilon_{n\ell}\sum_{ij} n_i\ell_j - \varepsilon_{\ell s}\sum_{ij}\ell_i s_j - \varepsilon_{ns}\sum_{ij} n_i s_j$$

where the sums run only over nearest neighbors on a rectangular 3D lattice, ℓ_i, n_i, and s_i are binary variables roughly proportional to the density of the solvent, NPs and substrate at site i, respectively (0 for low density or 1 for high density). ε_{ℓ}, ε_n, $\varepsilon_{n\ell}$, $\varepsilon_{\ell s}$, and ε_{ns} are the liquid−liquid, NP−NP, liquid−NP, liquid−substrate, NP−substrate interfacial energies, respectively, and μ is the chemical potential (for more details, see references).[16,35−37] The dynamics are stochastic both for solvent density fluctuations and for NP diffusion, where balance is preserved. The NPs undergo a random walk on the lattice, biased by their interactions. We attempt to displace a NP by single lattice spacing in a random direction every N_{ℓ} solvent moves (defined below), but only if the region into which the NP moves is completely filled with liquid. To mimic the low mobility of NPs we choose a large value for N_{ℓ} (typically 3 orders of magnitude larger than our previous simulations). Such a move is accepted with the Metropolis probability P_{acc} = min[1, exp(−$\beta\Delta H$)], where β is the inverse temperature and ΔH is the energy difference between the new and old configuration. Liquid moves are more evolved to include, in a primitive way, "dragging" of the NPs by the receding solvent front. We attempt to convert a randomly chosen lattice cell i_{rnd} occupied by the solvent ($\ell_{i_{rnd}} = 1 \rightarrow 0$), but only if at least one of the adjacent lattice cells contains vapor. In addition, if at least one of the neighboring cells is occupied by NPs, we attempt to "drag" the NP in the opposite direction of the cell i_{rnd} with a probability ξ (*i.e.*, not every evaporation move includes a dragging attempt), but only if the region into which the NP moves is filled with liquid. This evaporation/dragging move is accepted with a different Metropolis probability P_{acc} = min[1, exp(−$\beta\Delta H$)($n/\bar{n}$)], where $\bar{n}$ is the number of NPs adjacent to cell i_{rnd} and is the number of NPs that are allowed to move. Similarly, reverse moves are included for condensation with the corresponding Metropolis probability, preserving balance.

Conflict of Interest: The authors declare no competing financial interest.

Acknowledgment. Work on platinum nanocrystal synthesis, fabrication of liquid TEM cells, and TEM experiment and analysis was supported by the Physical Chemistry of Semiconductor Nanocrystals Program, KC3105, Director, Office of Science, Office of Basic Energy Sciences, of the United States Department of Energy under contract DE-AC02-05CH11231. E. Rabani thanks the FP7Marie Curie IOF project HJSC and the Miller Institute for Basic Research in Science at UC Berkeley for financial support *via* a Visiting Miller Professorship. H. Zheng thanks the funding support of Laboratory Directed Research Program at Lawrence Berkeley National Lab, funded by the U.S. Department of Energy under Contract No. DE-AC02-05CH11231 for support for her

work on liquid cell fabrication and paper revision. We acknowledge the support of National Center for Electron Microscopy, which are funded by the Director, Office of Science, Office of Basic Energy Sciences, Materials Science and Engineering Division of the U.S. Department of Energy under Contract No. DE-AC02-05CH11231. The authors thank D. Grauer and A. Widmer-Cooper for useful discussion.

Supporting Information Available: In-situ TEM video for superlattice formation, trajectories toward superlattice after thermal drift correction, *in situ* TEM video for individual NP's addition onto ordered domain, NPs tracking method, complete description of lattice gas model, TEM images and corresponding radial-distribution functions of NPs assemblies formed under electron beam irradiation and drop casting, simulated trajectory showing the full time range from an initial random phase to the assembled phase, simulated trajectories showing how NPs are dragged by the solvent front, additional plots of surface coverage and 2-D bond orientational order, TEM still snap-shots of domain growth by NP addition, simulated superlattice patterns with varying coverage of NPs under low NP diffusivity. This material is available free of charge *via* the Internet at http://pubs.acs.org.

REFERENCES AND NOTES

1. Bishop, K. J. M.; Wilmer, C. E.; Soh, S.; Grzybowski, B. A. Nanoscale Forces and Their Uses in Self-Assembly. *Small* **2009**, *5*, 1600–1630.
2. Baker, J. L.; Widmer-Cooper, A.; Toney, M. F.; Geissler, P. L.; Alivisatos, A. P. Device-Scale Perpendicular Alignment of Colloidal Nanorods. *Nano Lett.* **2010**, *10*, 195–201.
3. Li, F.; Josephson, D. P.; Stein, A. Colloidal Assembly: The Road from Particles to Colloidal Molecules and Crystals. *Angew. Chem., Int. Ed.* **2011**, *50*, 360–388.
4. Bigioni, T. P.; Lin, X. M.; Nguyen, T. T.; Corwin, E. I.; Witten, T. A.; Jaeger, H. M. Kinetically Driven Self Assembly of Highly Ordered Nanoparticle Monolayers. *Nat. Mater.* **2006**, *5*, 265–270.
5. Ohara, P. C.; Heath, J. R.; Gelbart, W. M. Self-Assembly of Submicrometer Rings of Particles from Solutions of Nanoparticles. *Angew. Chem., Int. Ed.* **1997**, *36*, 1078–1080.
6. Rabideau, B. D.; Pell, L. E.; Bonnecaze, R. T.; Korgel, B. A. Observation of Long-Range Orientational Order in Monolayers of Polydisperse Colloids. *Langmuir* **2007**, *23*, 1270–1274.
7. Rabani, E.; Reichman, D. R.; Geissler, P. L.; Brus, L. E. Drying-Mediated Self-Assembly of Nanoparticles. *Nature* **2003**, *426*, 271–274.
8. Kletenik-Edelman, O.; Ploshnik, E.; Salant, A.; Shenhar, R.; Banin, U.; Rabani, E. Drying-Mediated Hierarchical Self-Assembly of Nanoparticles: A Dynamical Coarse-Grained Approach. *J. Phys. Chem. C* **2008**, *112*, 4498–4506.
9. Sztrum, C. G.; Hod, O.; Rabani, E. Self-Assembly of Nanoparticles in Three-Dimensions: Formation of Stalagmites. *J. Phys. Chem. B* **2005**, *109*, 6741–6747.
10. Yosef, G.; Rabani, E. Self-Assembly of Nanoparticles into Rings: A Lattice-Gas Model. *J. Phys. Chem. B* **2006**, *110*, 20965–20972.
11. Tang, J.; Ge, G. L.; Brus, L. E. Gas−Liquid−Solid Phase Transition Model for Two-Dimensional Nanocrystal Self-Assembly on Graphite. *J. Phys. Chem. B* **2002**, *106*, 5653–5658.
12. Ge, G.; Brus, L. E. Evidence for Spinodal Phase in Two-Dimensional Nanocrystal Self-Assembly. *J. Phys. Chem. B* **2000**, *104*, 9573–9575.
13. Martin, C. P.; Blunt, M. O.; Pauliac-Vaujour, E.; Stannard, A.; Moriaty, P. Controlloing Pattern Formation in Nanoparticle Assemblies *via* Directed Solvent Dewetting. *Phys. Rev. Lett.* **2007**, *99*, 116103.
14. Kalsin, A. M.; Fialkowski, M.; Paszewski, M.; Smoukov, S. K.; Bishop, K. J. M.; Grzybowski, B. A. Electrostatic Self-Assembly of Binary Nanoparticle Crystals with a Diamond-like Lattice. *Science* **2006**, *312*, 420–424.
15. Kolny, J.; Kornowski, A.; Weller, H. Self-Organization of Cadmium Sulfide and Gold Nanoparticles by Electrostatic Interaction. *Nano Lett.* **2002**, *2*, 361–364.
16. Shevchenko, E. V.; Talapin, D. V.; Kotov, N. A.; O'Brien, S.; Murray, C. B. Structural Diversity in Binary Nanoparticle Superlattices. *Nature* **2006**, *439*, 55–59.
17. Korgel, B. A.; Fullam, S.; Connolly, S.; Fitzmaurice, D. Assembly and Self-Organization of Silver Nanocrystal Superlattices: Ordered "Soft Spheres". *J. Phys. Chem. B* **1998**, *102*, 8379–8388.
18. Denkov, N. D.; Velev, O. D.; Kralchevsky, P. A.; Ivanov, I. B.; Yoshimura, H.; Nagayama, K. Mechanism of Formation of 2-Dimensional Crystals from Latex-Particles on Substrates. *Langmuir* **1992**, *8*, 3183–3190.
19. Gasser, U.; Weeks, E. R.; Schofield, A.; Pusey, P. N.; Weitz, D. A. Real-Space Imaging of Nucleation and Growth in Colloidal Crystallization. *Science* **2001**, *292*, 258–262.
20. Grier, D. G.; Murray, C. A. The Microscopic Dynamics of Freezing in Supercooled Colloidal Fluids. *J. Chem. Phys.* **1994**, *100*, 9088–9095.
21. Murray, C. A.; Grier, D. G. Video Microscopy of Monodisperse Colloidal Systems. *Annu. Rev. Phys. Chem.* **1996**, *47*, 421–462.
22. Ramos, L.; Lubensky, T. C.; Dan, N.; Nelson, P.; Weitz, D. A. Surfactant-Mediated Two-Dimensional Crystallization of Colloidal Crystals. *Science* **1999**, *286*, 2325–2328.
23. Savage, J. R.; Blair, D. W.; Levine, A. J.; Guyer, R. A.; Dinsmore, A. D. Imaging the Sublimation Dynamics of Colloidal Crystallites. *Science* **2006**, *314*, 795–798.
24. Abecassis, B.; Testard, F.; Spalla, O. Gold Nanoparticle Superlattice Crystallization Probed *in Situ*. *Phys. Rev. Lett.* **2008**, *100*, 115504.
25. Ge, G. L.; Brus, L. E. Fast Surface Diffusion of Large Disk-Shaped Nanocrystal Aggregates. *Nano Lett.* **2001**, *1*, 219–222.
26. Jiang, Z.; Lin, X. M.; Sprung, M.; Narayanan, S.; Wang, J. Capturing the Crystalline Phase of Two-Dimensional Nanocrystal Superlattices in Action. *Nano Lett.* **2010**, *10*, 799–803.
27. Lee, B.; Podsiadlo, P.; Rupich, S.; Talapin, D. V.; Rajh, T.; Shevchenko, E. V. Comparison of Structural Behavior of Nanocrystals in Randomly Packed Films and Long-Range Ordered Superlattices by Time-Resolved Small Angle X-ray Scattering. *J. Am. Chem. Soc.* **2009**, *131*, 16386–16388.
28. Connolly, S.; Fullam, S.; Korgel, B.; Fitzmaurice, D. Time-Resolved Small-Angle X-ray Scattering Studies of Nanocrystal Superlattice Self-Assembly. *J. Am. Chem. Soc.* **1998**, *120*, 2969–2970.
29. de Jonge, N.; Ross, F. M. Electron Microscopy of Specimens in Liquid. *Nat. Nanotechnol.* **2011**, *6*, 695–704.
30. Ross, F. M.; Williamson, M. J.; Tromp, R. M.; Vereecken, P. M.; Hull, R. Dynamic Microscopy of Nanoscale Cluster Growth at the Solid−Liquid Interface. *Nat. Mater.* **2003**, *2*, 532–536.
31. Zheng, H. M.; Smith, R. K.; Jun, Y. W.; Kisielowski, C.; Dahmen, U.; Alivisatos, A. P. Observation of Single Colloidal Platinum Nanocrystal Growth Trajectories. *Science* **2009**, *324*, 1309–1312.
32. Tsung, C. K.; Kuhn, J. N.; Huang, W. Y.; Aliaga, C.; Hung, L. I.; Somorjai, G. A.; Yang, P. D. Sub-10 nm Platinum Nanocrystals with Size and Shape Control: Catalytic Study for Ethylene and Pyrrole Hydrogenation. *J. Am. Chem. Soc.* **2009**, *131*, 5816–5822.
33. Zheng, H. M.; Claridge, S. A.; Minor, A. M.; Alivisatos, A. P.; Dahmen, U. Nanocrystal Diffusion in a Liquid Thin Film Observed by *in Situ* Transmission Electron Microscopy. *Nano Lett.* **2009**, *9*, 2460–2465.
34. Elbaum, M.; Lipson, S. G. How Does a Thin Wetted Film Dry Up. *Phys. Rev. Lett.* **1994**, *72*, 3562–3565.
35. Sonnichsen, C.; Alivisatos, A. P. Gold Nanorods as Novel Nonbleaching Plasmon-Based Orientation Sensors for Polarized Single-Particle Microscopy. *Nano Lett.* **2005**, *5*, 301–304.
36. Steinhardt, P. J.; Nelson, D. R.; Ronchetti, M. Bond-Orientational Order in Liquids and Glasses. *Phys. Rev. B* **1983**, *28*, 784–805.
37. Wang, Z. R.; Alsayed, A. M.; Yodh, A. G.; Han, Y. L. Two-Dimensional Freezing Criteria for Crystallizing Colloidal Monolayers. *J. Chem. Phys.* **2010**, *132*, 154501.

38. Anderson, V. J.; Lekkerkerker, H. N. W. Insights into Phase Transition Kinetics from Colloid Science. *Nature* **2002**, *416*, 811–815.
39. Savage, J. R.; Dinsmore, A. D. Experimental Evidence for Two-Step Nucleation in Colloidal Crystallization. *Phy.s Rev. Lett.* **2009**, *102*, 198302.
40. Wolde, P. R.; Frenkel, D. Enhancement of Protein Crystal Nucleation by Critical Density Fluctuations. *Science* **1997**, *277*, 1975–1978.
41. Vekilov, P. G.; Galkin, O.; Chen, K.; Nagel, R. L.; Hirsch, R. E. Liquid−Liquid Separation in Solutions of Normal and Sickle Cell Hemoglobin. *Proc. Natl. Acad. Sci. USA* **2002**, *99*, 8479–8483.
42. Sztrum, C. G.; Rabani, E. Out-of-Equilibrium Self-Assembly of Binary Mixtures of Nanoparticles. *Adv. Mater.* **2006**, *18*, 565–571.
43. Egerton, R. F.; Li, P.; Malac, M. Radiation Damage in the TEM and SEM. *Micron* **2004**, *35*, 399–409.
44. Kralchevsky, P. A.; Denkov, N. D. Capillary Forces and Structuring in Layers of Colloid Particles. *Curr. Opin. Colloid. Interface Sci.* **2001**, *6*, 383–401.